First Assessment of SDGSAT-1 TIS Thermal Infrared Bands Calibration Using Landsat 9 TIRS-2

Min Zhu, Qiyao Wang, Jianing Yu, Zhuoyue Hu, and Fansheng Chen, *Senior Member, IEEE*

***Abstract*—SDGSAT-1, the inaugural Earth science satellite commissioned by the Chinese Academy of Sciences, successfully lifted off from China's Taiyuan Satellite Launch Center on 5 November 2021. Cross calibration has emerged as an indispensable methodology, providing an effective means for quality assessment, stability monitoring, and uncertainty analysis. This is achieved through the meticulous selection of an appropriate reference instrument. In our investigation, we conducted a comprehensive evaluation of the absolute radiometric calibration accuracy of the thermal infrared spectrometer (TIS), a pivotal component aboard SDGSAT-1. Our evaluation centered on a meticulous comparative analysis, where we juxtaposed the brightness temperature (BT) values recorded by TIS with the BT values derived from TIRS-2, computed following the spectral alignment with TIS. Our findings reveal that the current absolute BT bias for the *B*2 channel of TIS is less than 0.52 K. Meanwhile, the *B*3 channel exhibits a slightly larger fluctuation in absolute BT bias, yet remains within acceptable parameters, registering at less than 1 K. Notably, *B*3 emerges as the more dependable option for accurately gauging the temperature of the target region. Specifically, when the BT of *B*3 surpasses 290 K, the BT bias remains consistently below 0.3 K. In light of the approximately 40-min time difference in the water surface data utilized in our study, we conducted simulations to assess the channel BT of TIS under the scenario of a 0.25 °C water temperature variation. Our simulations conclusively demonstrate that the corresponding change in BT does not exceed 0.25 K.**

***Index Terms*—Cross calibration, thermal infrared (TIR), thermal infrared sensor 2 (TIRS-2), thermal infrared spectrometer (TIS).**

Manuscript received 19 November 2023; revised 19 January 2024; accepted 9 May 2024. Date of publication 13 May 2024; date of current version 23 May 2024. This work was supported in part by the Strategic Priority Research Program of the Chinese Academy of Sciences under Grant XDA19010102 and in part by the National Natural Science Foundation of China under Grant 61975222. *(Corresponding authors: Fansheng Chen; Zhuoyue Hu.)*

Min Zhu and Qiyao Wang are with the Key Laboratory of Intelligent Infrared Perception, Shanghai Institute of Technical Physics, Chinese Academy of Sciences, Shanghai 200083, China, and also with the University of Chinese Academy of Sciences, Beijing 100049, China (e-mail: zhumin@mail.sitp.ac.cn; wwangqiyao@163.com).

Jianing Yu is with the Hangzhou Institute for Advanced Study, University of Chinese Academy of Sciences, Hangzhou 310024, China, and also with the University of Chinese Academy of Sciences, Beijing 100049, China (e-mail: yujianing221@mails.ucas.ac.cn).

Zhuoyue Hu is with the Key Laboratory of Intelligent Infrared Perception, Shanghai Institute of Technical Physics, Chinese Academy of Sciences, Shanghai 200083, China (e-mail: huzhuoyue@mail.sitp.ac.cn).

Fansheng Chen is with the Key Laboratory of Intelligent Infrared Perception, Shanghai Institute of Technical Physics, Chinese Academy of Sciences, Shanghai 200083, China, also with the International Research Center of Big Data for Sustainable Development Goals (CBAS), Beijing 100094, China, and also with the Hangzhou Institute for Advanced Study, University of Chinese Academy of Sciences, Hangzhou 310024, China (e-mail: cfs@mail.sitp.ac.cn).

Digital Object Identifier 10.1109/JSTARS.2024.3400508

I. Introduction

CURRENTLY, cross calibration has emerged as a widely adopted technique for assessing the radiometric calibration accuracy of satellite sensors. Leveraging the superior hyperspectral characteristics and precise calibration standards, cross calibration of thermal infrared (TIR) channels relies heavily on infrared hyperspectral detectors from polar orbit satellites, such as IASI and CrIS [1], [2]. This process encompasses remote sensing data calibration and accuracy validation, facilitated through methods, such as simultaneous nadir overpass, as well as precise alignment in time, space, geometry, and spectral domains. Notable examples of this practice include cross-calibration efforts involving TIR channels on satellites, such as FY-4A AGRI [3] and HY-1C COCTS [4]. Additionally, the moderate-resolution imaging spectrometer aboard sun-synchronous orbit satellites Terra and Aqua has become a widely utilized reference satellite for cross calibration, extending its application to satellites, such as the FY series [5], HJ series satellite [6], [7], [8], [9], and GF series [10], [11] for TIR channel calibration.

SDGSAT-1, the first Earth science satellite launched by the Chinese Academy of Sciences, achieved a successful liftoff from China's Taiyuan Satellite Launch Center on 5 November 2021. Operating in a solar-synchronous orbit at an altitude of 505 km, with a 300-km-wide swath, SDGSAT-1 is equipped with three primary sensors: the thermal infrared spectrometer (TIS), the multispectral imager for inshore, and the glimmer imager for urbanization. It boasts the capability to provide global coverage in an 11-day cycle. TIS, in particular, is dedicated to the spatial mapping of surface thermal radiation. Comprising three long-wave TIR channels, namely *B*1 (8.0–10.5 μm), *B*2 (10.3–11.3 μm), and *B*3 (11.5–12.5 μm), TIS employs a long-wave time-delayed integration detector composed of four long-wave 512 $\times$ 4 $\times$ 3 HgCdTe infrared focal plane detector modules. These modules are thoughtfully staggered and assembled, as depicted in Fig. 1. A 25-pixel overlap is employed between every two adjacent modules, and each band pixel size measures 512 $\times$ 4. The four columns of photosensitive elements surrounding each band serve to mitigate edge effects [12]. The wide long-wave infrared channels offered by TIS are of paramount importance for the quantitative remote sensing applications related to the study of human activities and indicators pertaining to the natural environment.

TIS is equipped with a blackbody (BB) used as the reference standard for calibrating its TIR channels. Onboard radiometric calibration of the TIR channels is executed by collecting data

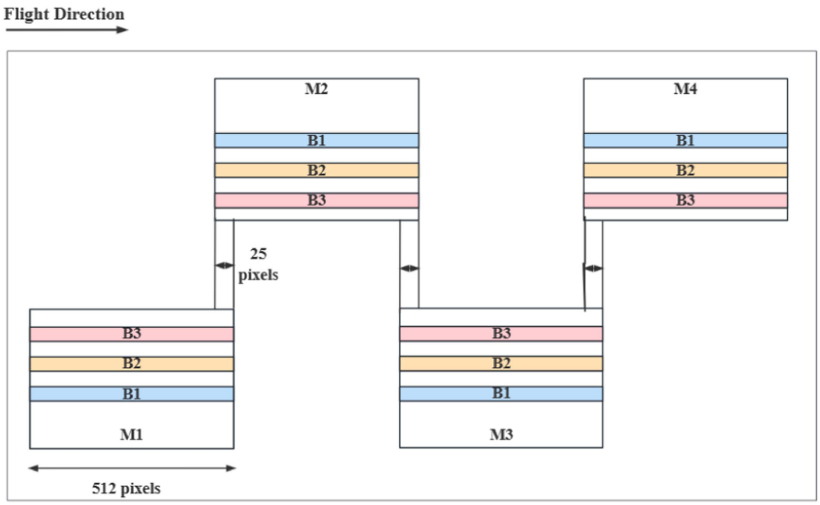

Fig. 1. TIS detector structure diagram.

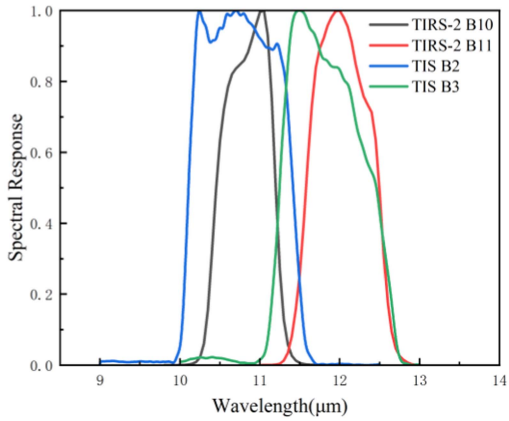

Fig. 2. SRFs of TIRS-2 and SDGSAT-1 TIS data.

from six sets of cold air observations and BB measurements. Ensuring the accurate monitoring of the calibration status of each TIS channel is essential for acquiring the high-quality data. Despite the presence of a calibration system for TISs TIR channels, regular performance monitoring of the onboard calibration system remains imperative for evaluating calibration accuracy.

Landsat 9 represents a substantial improvement over its predecessors, delivering enhanced radiometric and geometric performance [13], [14]. The thermal infrared sensor 2 (TIRS-2) on Landsat 9 operates as a push-broom imager, covering a 185-km-wide swath in a 705 km orbit with a field of view of ±7.5°. Notably, TIRS-2 features an upgraded stray light suppression structure compared with its predecessor, Landsat 8 TIRS [15], [16]. The onboard calibration uncertainty of TIRS-2 falls below 1.4% (or <1.0 K at 295 K) within its nominal temperature range of 260–330 K. TIRS-2 exhibits minimal in-orbit instability, approximately 0.025%, and offers a noise equivalent temperature difference of 0.08 K [17]. TIRS-2 provides two TIR channels with a pixel resolution of 100 m: $B10$ (10.6–11.19 μm) and $B11$ (11.5–12.51 μm) [18]. Fig. 2 illustrates the spectral response function (SRF) of TISs two TIR channels alongside the spectral coverage of Landsat 9 TIRS-2s TIR channels.

Table I presents a comparison of specific technical indicators between TIRS-2 and TIS. Notably, TIRS-2 and TIS exhibit overlapping spectral characteristics. TIRS-2 boasts stable and precise radiation and spectral performance, with minimal disparities in radiation calibration [19]. Therefore, TIRS-2 serves as a valuable reference sensor for evaluating the radiation performance of TIS within the same spectral range. However, it is worth noting that TIRS-2 does not fully encompass the SRF of TIS band $B1$ (8–10.5 μm); thus, the calibration accuracy of TIS band $B1$ is not assessed based on Landsat 9 TIRS-2 within the scope of this study.

II. Data and Methods

A. Data

Table II illustrates the spectral correspondence between TIRS-2 s $B10$ and $B11$ bands and TISs $B2$ and $B3$ bands, respectively. The cross-calibration experiment focuses on these two TIR channels of TIRS-2. In this investigation, we utilized TIS *L4* level data and Tier 1 Level-1 Precision Terrain (L1TP) processed data from TIRS-2 for the cross-calibration process.

The TIS L4 level data, which has undergone radiometric calibration and geometric projection processing, was sourced from the SDGSAT-1 satellite data sharing open system. The TIRS-2 L1TP data, characterized by well-defined radiometry and inter-calibration across various Landsat sensors, were accessed through the U.S. Geological Survey Earth Explorer.

Given the substantial heat capacity of water, their temperature variations over short time spans are relatively insignificant. To mitigate spatial matching errors and minimize the influence of atmospheric path differences on the brightness temperature (BT) comparison between the two sensors, we selected cloud-free remote sensing images of lakes and bays with a time gap of 40 min. These images were obtained by both TIS and TIRS-2 at the nadir point.

TABLE I
INSTRUMENT CHARACTERISTICS OF SDGSAT-1 TIS AND LANDSAT 9 TIRS-2

	LANDSAT 9 TIRS-2	SDGSAT-1 TIS
Orbital Altitude	705 km	505 km
Swath	185 m	300 km
Spatial Resolution	100 m	30 m
Spectral Coverage	B10: 10.6–11.19 μm B11: 11.5–12.51 μm	B1: 8.0–10.5 μm B2: 10.3–11.3 μm B3: 11.5–12.5 μm
Sensitivity (@300 K) (Prelaunch Performance)	B10: 0.05 K B11: 0.07 K	B1: 0.034 K B2: 0.047 K B3: 0.076 K

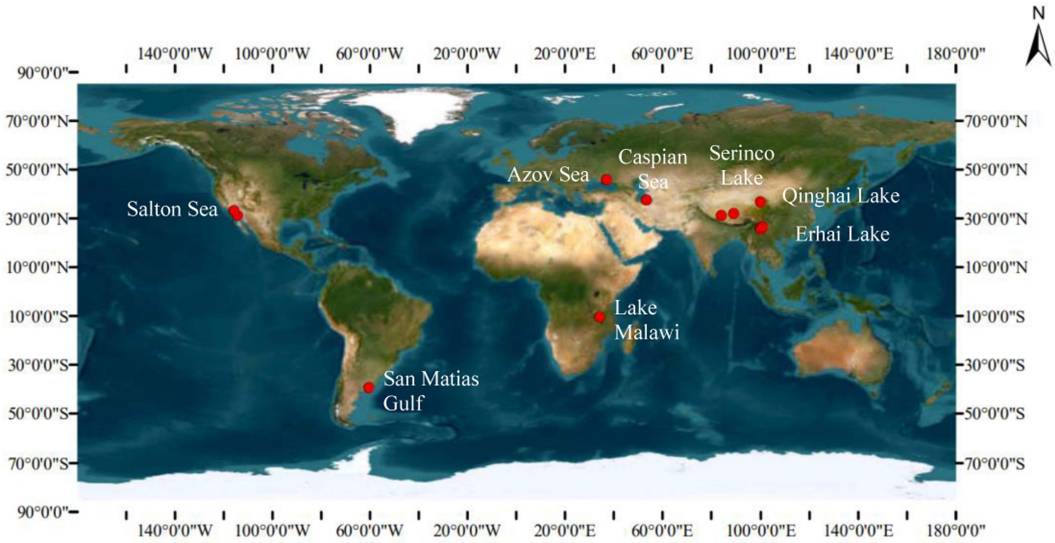

Fig. 3. Test regions (red points) of cross-calibration assessment.

TABLE II
VALUES OF SPECTRAL MATCHING FACTORS

Band	k	b	R^2
B2	1.0100056	–0.0982982	0.99998
B3	1.0726715	–0.4520002	0.99999

In the process of selecting TIRS-2 and TIS data, several conditions were met. First, the imaging time interval between TIRS-2 and TIS was less than 40 min in identical calibration experimental areas. Second, there was no cloud cover above the radiometric correction field. Notably, since water temperatures exhibit significant diurnal variations, observations from both satellites were further restricted to time ranges when water temperatures remain relatively stable during the day. The experiment encompassed synchronous observations from SDGSAT-1 TIS and LANDSAT 9 TIRS-2 spanning from February 2022 to January 2023. The specific test locations are depicted as red dots in Fig. 3, encompassing Erhai Lake and Qinghai Lake in China, along with the Salton Sea in the United States, serving as the primary test regions.

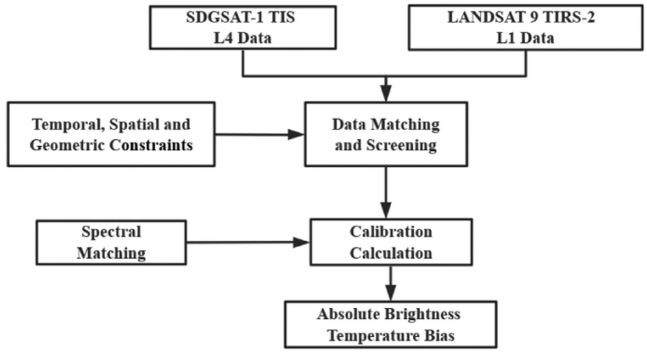

Fig. 4. Cross-calibration assessment flowchart of TIS.

B. Spatial Matching

The cross-calibration procedure, as illustrated in Fig. 4, encompasses several fundamental stages. First, it involves meticulous data matching and screening within the cross-observation area of the two satellites, striving to achieve optimal alignment in terms of time, space, and observation geometry. This represents a pivotal initial phase in the cross-calibration process, directly

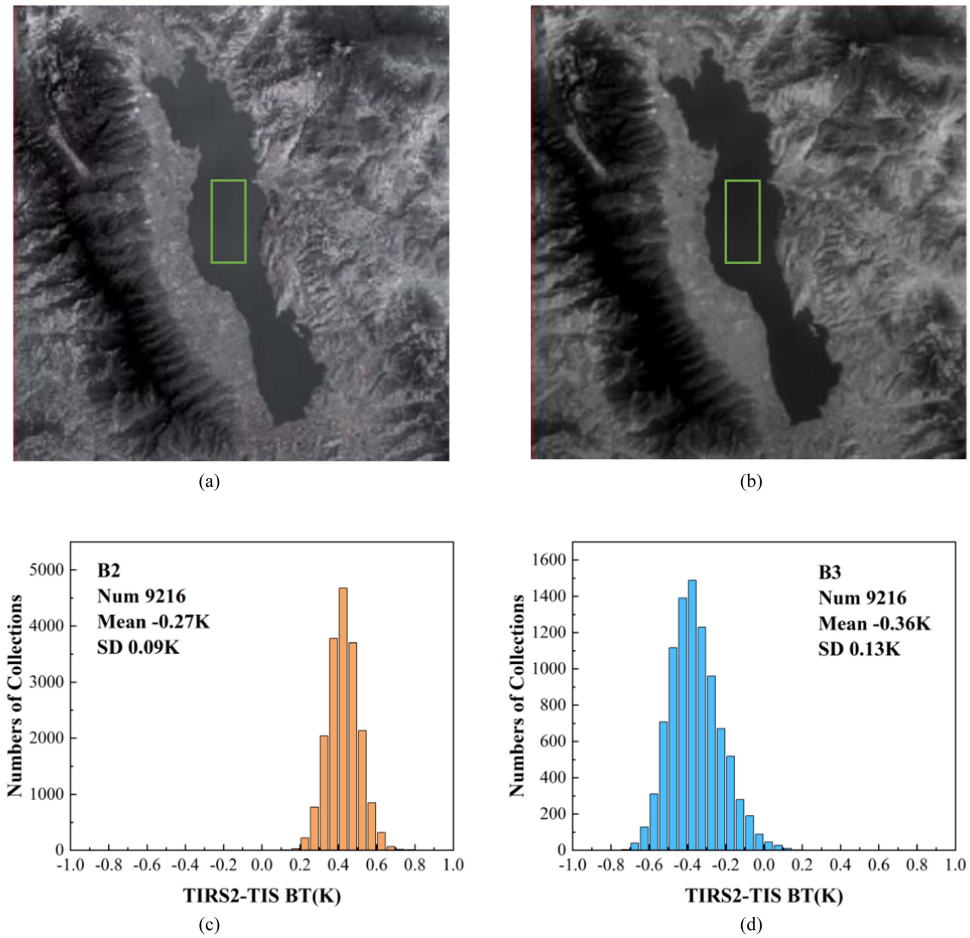

Fig. 5. Statistical chart of absolute BT bias of green rectangular area of Erhai Lake on 2 March 2022. (a) TIS image. (b) TIRS-2 *B*10 image. (c) Statistical chart of absolute BT bias of *B*2. (d) Statistical chart of absolute BT bias of *B*3.

influencing both calculation efficiency and calibration accuracy. Subsequently, the matched sample data from the two instruments are transformed into a directly comparable format, entailing unit conversions and spectral convolution or spectral compensation processes. Finally, a comparative analysis is conducted on the BT data acquired from TIS and TIRS-2.

TIS boasts a spatial resolution of 30 m, while the LANDSAT 9 TIRS-2 operates at a spatial resolution of 100 m. To facilitate spatial matching, the original TIS digital number (DN) image at 30-m resolution is resampled to 100 m. In the process of spatial matching, areas characterized by uniformity are chosen to mitigate errors stemming from pixel resolution differences. The criterion for selecting these uniform regions is that the standard deviation of the DN is less than 1% of the mean DN. Spatial matching is executed based on the latitude and longitude, and due to the even distribution of the selected areas, any potential impact on the ultimate cross-calibration results can be considered negligible.

C. Spectral Matching

Due to disparities in the SRFs of the response channels between TIRS-2 and TIS, these two sensors yield differing channel radiance outputs for the same spectral radiance input. Consequently, prior to cross calibration, spectral matching is essential for the TIR channels monitored by both sensors to minimize the impact of spectral variations on radiance.

For precise spectral matching, we employed the high-fidelity spectral prediction capabilities of the moderate-spectral-resolution atmospheric transmittance model (MODTRAN) fine spectral-resolution model [20]. MODTRAN was utilized to simulate the radiance at the top of the atmosphere (TOA) under various atmospheric profiles. Subsequently, the SRFs corresponding to the channels of TIRS-2 and TIS were convolved with the simulated TOA radiance data to derive comparable channel radiance values. The calculation of normalized channel radiance for the corresponding channels of TIRS-2 and TIS is conducted as follows:

$$L_{\mathrm{TIRS2}} = \frac{\int L_S(\lambda)\, f_{\mathrm{TIRS2}}(\lambda)\, d\lambda}{\int f_{\mathrm{TIRS2}}(\lambda)\, d\lambda} \tag{1}$$

$$L_{\mathrm{TIS}} = \frac{\int L_S(\lambda)\, f_{\mathrm{TIS}}(\lambda)\, d\lambda}{\int f_{\mathrm{TIS}}(\lambda)\, d\lambda} \tag{2}$$

where $L_S(\lambda)$ is the TOA radiance simulated by MODTRAN under different boundary layer temperatures (from 280 to 320 K) with various satellite viewing angles (vertical observation or inclined by 5°), using two standard midlatitude atmospheric

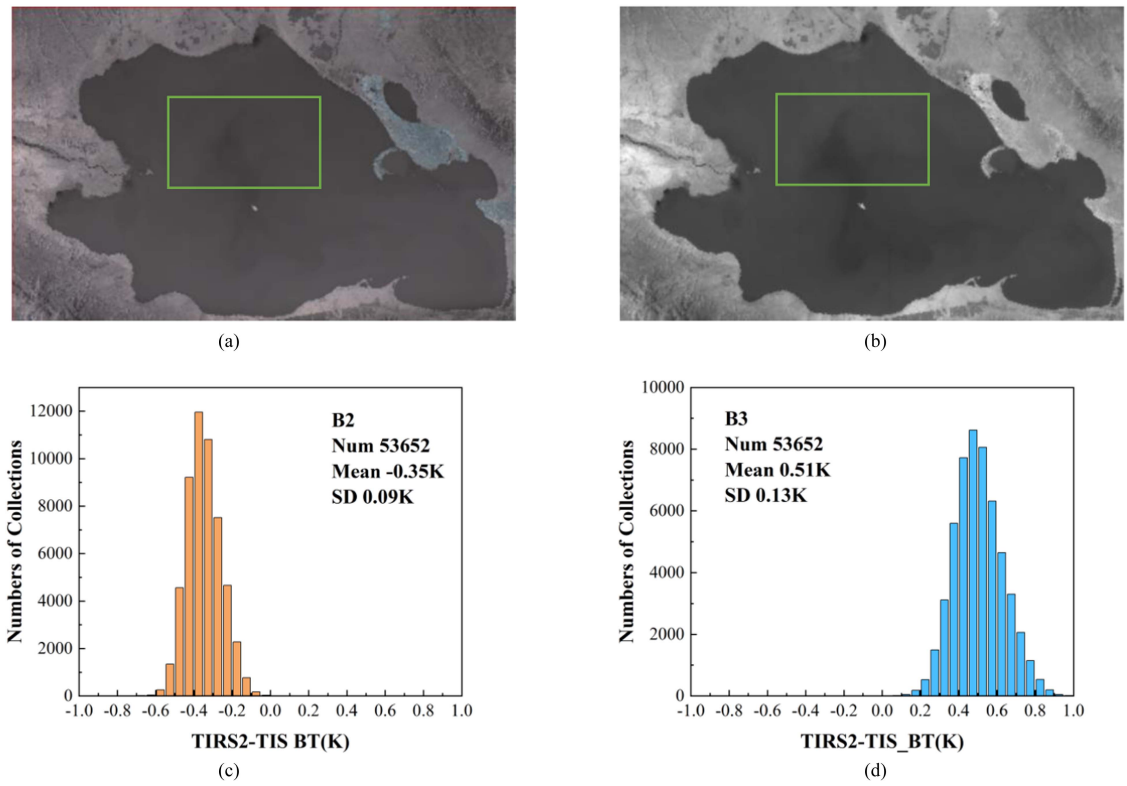

Fig. 6. Statistical chart of absolute BT bias of green rectangular area of Qinghai Lake on 22 July 2022. (a) TIS image. (b) TIRS-2 *B*10 image. (c) Statistical chart of absolute BT bias of *B*2. (d) Statistical chart of absolute BT bias of *B*3.

profiles (winter and summer). $f_{\mathrm{TIRS2}}(\lambda)$ is the TIRS-2 SRF, and $f_{\mathrm{TIS}}(\lambda)$ is the TIS SRF.

Linear regression was performed on the obtained multiple sets of L_{TIRS2} and L_{TIS} to obtain the spectral matching factor. After spectral matching, the radiance of the TIRS2 TIR channel is converted to the TIR channel radiance of TIS. The radiance of TIS for cross comparison can be expressed by spectral matching factors k and b

$$L_{\mathrm{TIS}}{}' = k \cdot L_{\mathrm{TIRS2}}{}' + b \tag{3}$$

where $L_{\mathrm{TIRS2}}{}'$ can be calculated by the officially given radiometric calibration coefficient. The values of k and b are listed in Table II and R^2 is the goodness of fit of (3).

D. Absolute BT Difference Calculation

BT can be calculated using the radiance with the Planck function

$$\mathrm{BT} = \frac{K_2}{\ln\left(\frac{K_1}{L} + 1\right)} \tag{4}$$

where the specific values of K_1 and K_2 are shown in Table III.

The accuracy of cross calibration is represented by the absolute BT difference between TIS and TIRS-2

$$\Delta\mathrm{BT} = \mathrm{BT}_{\mathrm{TIS}} - \mathrm{BT}_{\mathrm{TIS}'} \tag{5}$$

where $\mathrm{BT}_{\mathrm{TIS}}$ is the brightness temperature of TIS calculated by the official BB calibration coefficient according to the Planck function, and $\mathrm{BT}_{\mathrm{TIS}'}$ is the brightness temperature calculated from (3) according to the Planck formula.

TABLE III
VALUES OF K_1 AND K_2

Band	K_1 / mW · cm^{-2} · sr^{-1} · μm^{-1}	K_2/K
B2	838.7063	1342.7187
B3	543.058	1232.0214

III. Results and Discussion

A. TIRS2-TIS Absolute BT Difference

In this study, we have opted to employ daytime water temperature data spanning from February 2022 to January 2023 to assess the calibration accuracy of TIS.

Table IV presents the absolute BT difference for band *B*3, which registers at 0.69 K on 22 February 2022. The BT in the *B*3 spectral band typically hovers around 259 K. Given the substantial nonlinearity errors at the low-temperature end of TIS, such discrepancies still fall within the permissible error range.

Figs. 5, 6, and 7, panels (a) and (b), delineate the computation area enclosed within a green box. Panels (c) and (d) provide statistical information regarding the number of samples utilized in the analysis. The BT bias for the TIS-measured BT at the locations, as indicated in Fig. 5, is detailed in Table IV, spanning a broad BT spectrum from 260 to 298 K. The data indicate that the BT error of the thermal imager's *B*2 channel exhibits relatively consistent stability, with the majority of deviations falling below 0.5 K. The maximum BT discrepancy for *B*2 stands

TABLE IV
MEAN AND SD OF ABSOLUTE BT DIFFERENCE OF THE TEST SITES IN FIG. 2

Observation Area	Observation Time (UTC)	B2 Mean(K)	B2 SD(K)	B3 Mean(K)	B3 SD(K)
Serinco Lake	TIS: 2022.02.22 03:55:24 TIRS2: 2022.02.22 04:34:54	0.25@259.7	0.14	−0.69@259.1	0.18
Erhai Lake	TIS: 2022.03.02 03:10:58 TIRS2: 2022.03.02 03:46:57	−0.27@283.7	0.09	−0.36@283.2	0.13
Beibu Gulf	TIS: 2022.04.11 02:27:46 TIRS2: 2022.04.11 02:59:23	0.40@293.4	0.08	−0.10@292.8	0.11
Caspian Sea	TIS: 2022.04.19 06:19:11 TIRS2: 2022.04.19 07:01:19	−0.29@288.6	0.10	−0.50@288.4	0.10
Azov Sea	TIS: 2022.05.16 07:42:01 TIRS2: 2022.05.16 08:19:03	0.45@286.8	0.10	0.16@286.0	0.16
Serinco Lake	TIS: 2022.05.29 03:52:09 TIRS2: 2022.05.29 04:34:18	−0.52@285.9	0.17	−0.61@285.1	0.18
Gulf of California	TIS: 2022.06.26 17:33:48 TIRS2: 2022.06.26 18:10:28	−0.30@298.0	0.12	−0.16@296.3	0.16
Qinghai Lake	TIS: 2022.07.22 03:21:29 TIRS2: 2022.07.22 03:56:02	−0.35@287.7	0.09	0.51@287.3	0.13
Lake Malawi	TIS: 2022.10.06 07:12:22 TIRS2: 2022.10.06 07:52:06	−0.22@295.2	0.14	0.29@294.3	0.18
San Matias Gulf	TIS: 2022.11.22 07:12:22 TIRS2: 2022.11.22 07:52:06	0.21@287.2	0.19	0.78@286.6	0.21
Salton Sea	TIS: 2023.01.27 17:42:13 TIRS2: 2023.01.27 18:16:47	0.43@284.8	0.08	0.70@284.4	0.14

TABLE V
CROSS-CALIBRATION RESULTS AND THE OFFICIAL CALIBRATION COEFFICIENTS OF TIS SENSOR

Coefficient	B2 Gain	B2 Offset	B3 Gain	B3 Offset
Cross Calibration	0.00369	0.6718	0.00516	0.46703
Official Calibration	0.003946	0.124622	0.005329	0.22253
Relative Errors	6.48758 %	—	3.17133 %	—

at 0.52 K. Conversely, the *B*3 channel shows a slightly greater degree of fluctuation; however, for the most part, the BT error remains under 0.51 K until November 2022. On the whole, the absolute BT bias for TIS remains within the 1 K range.

The bias in BT exhibited by both TIS and TIRS-2 is contingent upon the target temperature, with smaller and more consistent biases observed at higher BT values, particularly for band *B*3. Specifically, the BT bias for *B*3 remains below 0.3 K when the BT of *B*3 exceeds 290 K.

B. Cross-Calibration Results

Using the linear fitting method, we aggregated all the corresponding data points extracted from image pairs captured over the Azov Sea on 16 May 2022 and the Gulf of California on 26 June 2022, in order to derive the cross-calibration coefficient. The detailed results are presented in Fig. 8, while the outcomes of the cross-calibration process are tabulated in Table V.

For the *B*2 and *B*3 spectral bands, the relative gain errors stand at 6.487582% and 3.17133%, respectively. It is worth noting that the gain relative error, as reported in Table V, remains below the 6.5% threshold, indicating the robust stability of the TIS cross calibration with Landsat-9 TIRS-2.

C. Systematic Error Assessment

The dynamic range of TIRS-2 spans from 220 to 340 K. Within this range, temperatures falling between 260 and 320 K are considered the nominal temperature range, while temperatures spanning from 220 to 260 K and from 320 to 340 K are categorized as the extended temperature range. It is worth noting that the onboard calibration uncertainty is significantly higher in the extended temperature regions compared with that within the nominal range. A radiometric uncertainty of 2% within the nominal range translates to approximately 1.2 K and 1.9 K in BT uncertainty for TIRS-2 channels *B*10 and *B*11, respectively. In the extended range, a 4% radiometric uncertainty corresponds to roughly 3.2 and 3.6 K BT uncertainty for the same channels. Various factors contribute to the on-orbit uncertainties of TIRS-2, including linearization, spectral response, TIRS-2 noise, radiometric reproducibility of the onboard calibrator (OBC), OBC temperature, fitting, and angular variability. In the nominal temperature range, the total on-board uncertainty stands at approximately 1.3% for both bands 10 and 11, while in the

TABLE VI
BT BIAS OF TIS VARIES WITH WATER TEMPERATURE IN MIDLATITUDE SUMMER AND WINTER

Water Temperature	TIS Band	BT(K) (Midlatitude summer)	ΔBT(K) (Midlatitude summer)	BT(K) (Midlatitude winter)	ΔBT(K) (Midlatitude winter)
10 ℃	B2	283.89	0.1637	281.09	0.2287
	B3	284.10	0.1352	280.52	0.2200
15 ℃	B2	287.20	0.1664	285.68	0.2293
	B3	286.83	0.1378	284.93	0.2208
25 ℃	B2	293.95	0.1712	294.88	0.2306
	B3	292.44	0.1425	293.79	0.2223

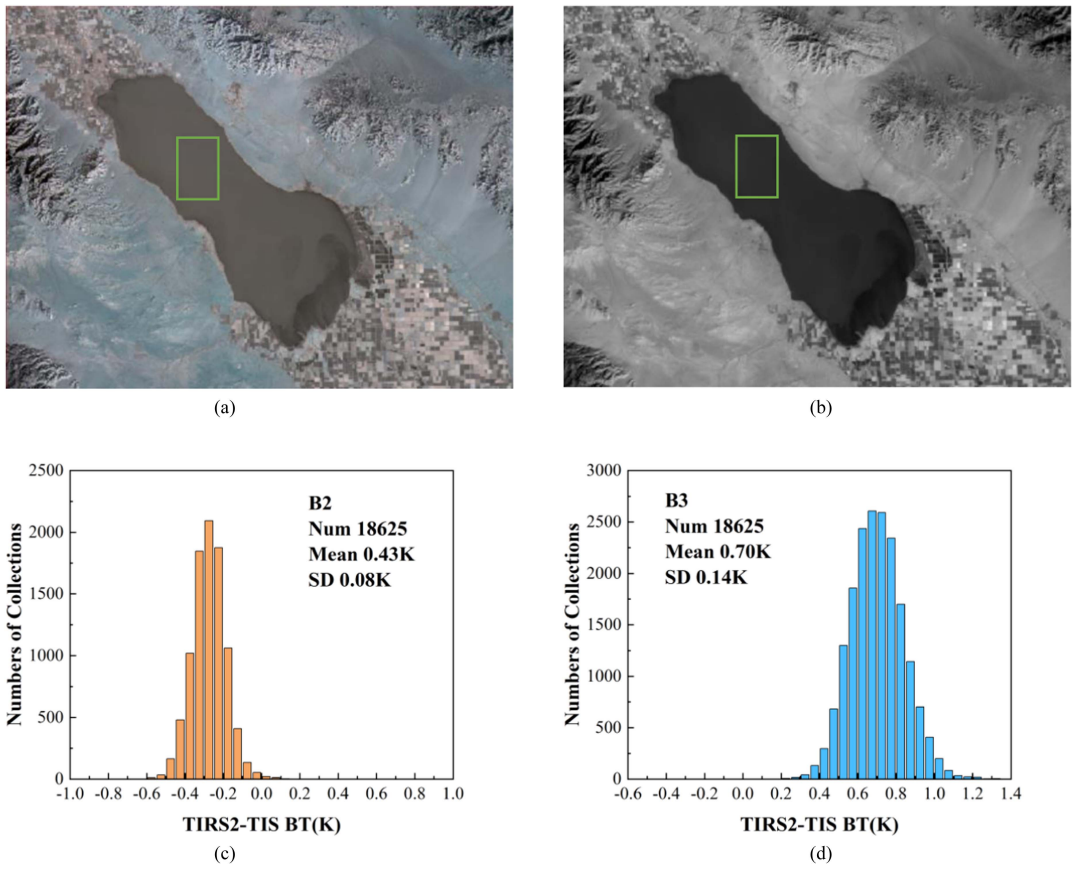

Fig. 7. Statistical chart of absolute BT bias of green rectangular area of Salton Sea on 27 January 2023. (a) TIS image. (b) TIRS-2 *B*10 image. (c) Statistical chart of absolute BT bias of *B*2. (d) Statistical chart of absolute BT bias of *B*3.

extended range, it is approximately 1.7% for band 10 and 1.5% for band 11 [16].

Indeed, in addition to the uncertainties arising from the reference sensor itself, the errors stemming from temporal disparities must not be overlooked. When conducting cross calibrations for satellites in geostationary orbits, data screening involves setting a time difference threshold of 10 min. This practice effectively mitigates the influence of atmospheric and temperature fluctuations on the cross-calibration process. In the case of SDGSAT-1 and Landsat 9, both belonging to the sun-synchronous orbit satellite category, the revisit periods for ground targets are approximately 11 days and 16 days, respectively. However, given the specific focus on lake or bay data in this study, the data selection process was further refined, resulting in the chosen datasets exhibiting a time difference of approximately 40 min.

We performed a cross-calibration error analysis on water surface data at temperatures of 10 °C, 15 °C, and 25 °C, with the objective of clarifying the influence of water temperature variations on channel BTs. We considered a scenario in which

TABLE VII
BT BIAS OF TIS CAUSED BY NAVIGATION AND GEOMETRIC MISMATCHES

	Longitudinal BT Bias (K)	Latitudinal BT Bias (K)	Geometric BT Bias (K)
B2	0.0012	0.0025	0.0418
B3	0.0011	0.0029	0.0379

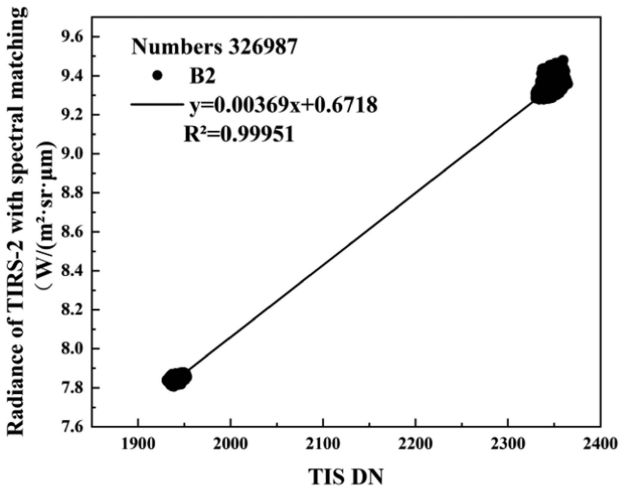

(a)

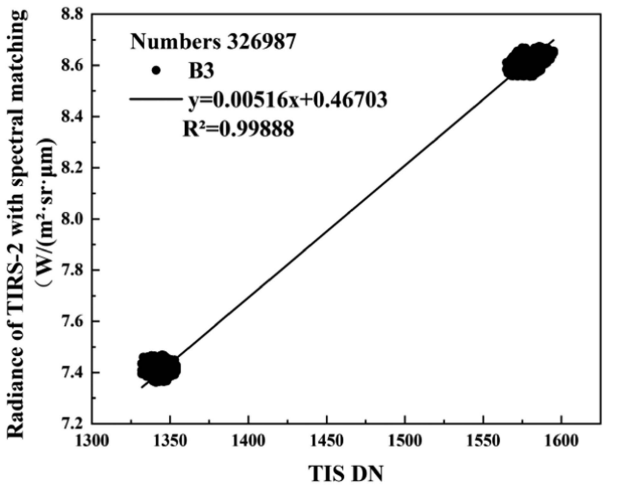

(b)

Fig. 8. Linear fitting of cross calibration. (a) Band 2 of TIS. (b) Band 3 of TIS.

the water surface temperature experiences a 1-h change during the day, with fluctuations remaining below 0.25 °C. Employing MODTRAN, we simulated water temperatures for midlatitude summer and winter conditions and assessed the consequent changes in channel BTs of TIS, as outlined in Table VI.

Table VI provides insights into the BT variations in TIS. During midlatitude summer, we observe a BT change of approximately 0.17 K for TIS *B*2 band and approximately 0.14 K for *B*3 band. Conversely, in midlatitude winter, these changes are slightly more pronounced, with TIS *B*2 band exhibiting a change of about 0.23 K and *B*3 band showing a change of around 0.22 K. It is noteworthy that during midlatitude winter, the BT variations are slightly more substantial compared with those in midlatitude summer. In summary, the temporal deviations introduce BT changes that do not exceed 0.25 K.

Table VII provides a comprehensive summary of errors introduced during the collocation steps, encompassing navigation and geometric discrepancies between TIS and TIRS-2. Navigation errors, encompassing both longitudinal and latitudinal BT biases, are calculated by averaging the BT bias across adjacent pixels in the target region of the TIS image. Geometric mismatch impacts the BT of TIS, primarily due to surface emissivity variations. To quantify these biases, we utilized MODTRAN simulations under varying atmospheric conditions and water albedo.

In Table VII, it becomes evident that BT is more sensitive to latitudinal mismatches compared with longitudinal mismatches, contributing an approximate 0.003 K to the BT bias of TIS. The most substantial BT bias is observed in the case of *B*2 channel, reaching 0.0418 K due to geometric mismatch. However, it is worth noting that the BT bias for both *B*2 and *B*3 channels remains under 0.05 K, rendering it negligible in subsequent data matching processes.

IV. CONCLUSION

In this study, we utilized 11 months of Landsat 9 TIRS-2 data to assess the radiation observations of the SDGSAT-1 TIS TIR channels *B*2 and *B*3. Landsat 9 TIRS-2 demonstrates high on-orbit calibration accuracy, making it a suitable reference for evaluating the radiation performance of TIS. Our approach began by selecting TIS and large-scale water data from TIRS-2, ensuring temporal, spatial, and geometric consistency in the cross-calibration observation area. Subsequently, we leveraged MODTRAN simulations to obtain hyperspectral data, which were convolved with the SRFs of TIS and TIRS-2, yielding spectral matching factors. By comparing the BT calculated using these factors with the BT obtained through BB calibration of TIS, we determined that the absolute BT bias for TISs *B*2 channel currently remains below 0.52 K. While exhibiting slightly greater fluctuations, *B*3 maintains an absolute BT bias of less than 1 K. Notably, *B*3 demonstrates enhanced reliability regarding temperature measurements within the target region, particularly with BTs exceeding 290 K. We conducted simulations to assess TISs sensor-reaching BT in response to a 0.25 °C water temperature change, considering a data time difference of approximately 40 min. The results indicate that the temperature-induced errors do not exceed 0.25 K.

This article evaluated the on-orbit calibration accuracy of the TIR channels of the thermal imager using available data from February 2022 to January 2023. For future research, we may explore the possibility of utilizing other high-precision on-orbit satellite sensors for cross calibrating the TIR *B*1 band and employ long-term on-orbit data to assess its stability over extended periods.

ACKNOWLEDGMENT

The authors would like to thank the International Research Center of Big Data for Sustainable Development Goals and the National Space Science Center, Chinese Academy of Sciences, for generously sharing the TIS data, and also the U.S. Geological Survey for providing the Landsat 9 TIRS-2 data. It is important to note that the views expressed in this article solely represent those of the authors.

REFERENCES

[1] T. J. Hewison et al., "GSICS inter-calibration of infrared channels of geostationary imagers using Metop/IASI," *IEEE Trans. Geosci. Remote Sens.*, vol. 51, no. 3, pp. 1160–1170, Mar. 2013.
[2] Y. Li, X. Xiong, J. McIntire, and A. Wu, "Comparison of the MODIS and VIIRS thermal emissive band radiometric calibration," *IEEE Trans. Geosci. Remote Sens.*, vol. 58, no. 7, pp. 4852–4859, Jul. 2020.
[3] X. He, N. Xu, X. Feng, X. Hu, H. Xu, and Y. Peng, "Assessing radiometric calibration of FY-4A/AGRI thermal infrared channels using CrIS and IASI," *IEEE Trans. Geosci. Remote Sens.*, vol. 60, 2022, Art. no. 5514512.
[4] M. Liu, L. Guan, J. Liu, Q. Song, C. Ma, and N. Li, "First assessment of HY-1C COCTS thermal infrared calibration using MetOp-B IASI," *Remote Sens.*, vol. 13, no. 4, Feb. 2021, Art. no. 635.
[5] Y. Li, J. Wu, and Y. Fang, "Cross-calibration of FY-3A/VIRR thermal infrared channel with TERRA/MODIS," *J. Atmos. Ocean. Technol.*, vol. 11, no. 3, pp. 204–210, 2016.
[6] J. Li et al., "Hj-1a thermal infrared band cross-calibration and validation," in *Proc. IEEE Int. Geosci. Remote Sens. Symp.*, 2009, pp. III–865–III–868.
[7] W. Liu, J. Li, Q. Han, L. Zhu, H. Yang, and Q. Cheng, "Orbital lifetime (2008-2017) radiometric calibration and evaluation of the HJ-1B IRS thermal infrared band," *Remote Sens.*, vol. 12, no. 15, Aug. 2020, Art. no. 2362.
[8] K. Sun, Q. Fu, and X. Qi, "Radiometric cross-calibration of thermal infrared channel of IRS sensor on HJ-1B satellite," *Infrared Laser Eng.*, vol. 39, no. 5, pp. 785–790, 2010.
[9] K. Li et al., "Radiometric cross calibration of China HJ-1B and MODIS thermal infrared channels using an SNO method based on observation elements matching," in *Proc. IEEE Int. Geosci. Remote Sens. Symp.*, 2021, pp. 7763–7766.
[10] X. Ye et al., "Cross-calibration of Chinese Gaofen-5 thermal infrared images and its improvement on land surface temperature retrieval," *Int. J. Appl. Earth Observ. Geoinf.*, vol. 101, Sep. 2021, Art. no. 102357.
[11] X. Zhou, D. Feng, Y. Xie, Z. Tao, T. Lv, and J. Wang, "Radiometric cross-calibration of GF-4/IRS based on MODIS measurements," *IEEE J. Sel. Topics Appl. Earth Observ. Remote Sens.*, vol. 14, pp. 6807–6814, Jun. 2021.
[12] Z. Hu, M. Zhu, Q. Wang, X. Su, and F. Chen, "SDGSAT-1 TIS prelaunch radiometric calibration and performance," *Remote Sens.*, vol. 14, no. 18, Sep. 2022, Art. no. 4543.
[13] G. Gross, D. Helder, C. Begeman, L. Leigh, M. Kaewmanee, and R. Shah, "Initial cross-calibration of Landsat 8 and Landsat 9 using the simultaneous underfly event," *Remote Sens.*, vol. 14, no. 10, May 2022, Art. no. 2418.
[14] J. A. Barsi, J. R. Schott, S. J. Hook, N. G. Raqueno, B. L. Markham, and R. G. Radocinski, "Landsat-8 thermal infrared sensor (TIRS) vicarious radiometric calibration," *Remote Sens.*, vol. 6, no. 11, pp. 11607–11626, Nov. 2014.
[15] B. Markham et al., "Landsat 9: Mission status and prelaunch instrument performance characterization and calibration," in *Proc. IEEE Int. Geosci. Remote Sens. Symp.*, 2019, pp. 5788–5791.
[16] A. Pearlman et al., "Prelaunch radiometric calibration and uncertainty analysis of Landsat thermal infrared sensor 2," *IEEE Trans. Geosci. Remote Sens.*, vol. 59, no. 4, pp. 2715–2726, Apr. 2021.
[17] A. Pearlman, B. Efremova, M. Montanaro, A. Lunsford, D. Reuter, and J. McCorkel, "Landsat 9 thermal infrared sensor 2 on-orbit calibration and initial performance," *IEEE Trans. Geosci. Remote Sens.*, vol. 60, Jun. 2022, Art. no. 1002608.
[18] B. Markham et al., "Landsat 9 mission update and status," *Proc. SPIE*, vol. 11501, 2020, Art. no. 115010O.
[19] G. Chander, T. J. Hewison, N. Fox, X. Wu, X. Xiong, and W. J. Blackwell, "Overview of intercalibration of satellite instruments," *IEEE Trans. Geosci. Remote Sens*, vol. 51, no. 3, pp. 1056–1080, Mar. 2013.
[20] A. Berk et al., "MODTRAN (TM) 5: 2006 update," *Proc. SPIE*, 2006.

Min Zhu received the B.S. degree in communication engineering from the Ocean University of China, Qingdao, China, in 2019. She is currently working toward the Ph.D. degree in electronic circuits and systems with the Shanghai Institute of Technical Physics, Chinese Academy of Sciences, Shanghai, China, and the University of Chinese Academy of Sciences, Beijing, China.

Her current research interests include the radiometric calibration method of multidimensional photoelectric system and cross calibration.

Qiyao Wang recieved the B.S. degree in electronic information science and technology from Beijing Forestry University, Beijing, China, in 2021. She is currently working toward the Ph.D. degree in electronic circuits and systems with the Shanghai Institute of Technical Physics, Chinese Academy of Sciences, Shanghai, China.

Her research interests include infrared radiometric calibration and infrared astronomical telescope.

Jianing Yu recieved the B.S. degree in telecommunications engineering from the Beijing University of Posts and Telecommunications, Beijing, China, in 2022. She is currently working toward the Ph.D. degree in electronic information with the Hangzhou Institute for Advanced Study, Chinese Academy of Sciences, Hangzhou, China. Her research focuses on infrared target detection.

Her research interest focuses on infrared target detection.

Zhuoyue Hu received the B.S. degree in information display and optoelectronic technology from the University of Electronic Science and Technology of China, Chengdu, China, in 2016, and the Ph.D. degree in physical electronics from the Shanghai Institute of Technical Physics, Chinese Academy of Sciences, Shanghai, China, in 2021.

Her research interests include radiometric calibration of remote sensing satellites.

Fansheng Chen (Senior Member, IEEE) received the B.S. degree in optoelectronic information engineering from Shandong University, Jinan, China, in 2002, and the Ph.D. degree in physical electronics from the Shanghai Institute of Technical Physics, Chinese Academy of Sciences, Shanghai, China, in 2007.

Since 2013, he has been a Professor with the Shanghai Institute of Technical Physics, Chinese Academy of Sciences. His research interests include the design of spatial high-resolution remote sensing and detection payloads, high-speed and low-noise information acquisition technology, and infrared dim small target detection technology. Meanwhile, he has been committed to the research and development of the space infrared staring detection instruments, the high spatial and temporal resolution photoelectric payloads, and the application of infrared multispectral information acquisition technology in artificial intelligence, target recognition, and other relative aspects.